Methods and apparatus for comprehensive characterization of performance attributes and limits of ultrafast laser optics

K. R. P. Kafka,* T. Z. Kosc, and S. G. Demos
Laboratory for Laser Energetics, University of Rochester, 250 East River Road, Rochester, NY 14623-1299, USA

Abstract. It is presently well understood that the operational performance limits of optics are determined by three fundamental attributes: the initiation of laser-induced damage, the growth of damage sites, and the transient (nondamaging) modification of optical parameters. The comprehensive characterization of the performance limitations of ultrafast optics requires consideration of all three fundamental attributes. The vast majority of literature to date, however, has focused primarily on damage-initiation and testing systems that are largely focused on determining the damage-initiation threshold under single- and multipulse excitation. In this work, we discuss a testing apparatus that was designed to offer the capability to adequately characterize all three of these performance attributes under femtosecond, near-infrared laser irradiation. Key aspects of methodology are discussed, including high-dynamic-range energy control, variable beam size, wavelength tunability, *B*-integral management, and functional performance characterization to explore the true operational limits of the components. Example results for a metal-dielectric mirror demonstrate the test station's operation.

Keywords: Damage testing systems, femtosecond lasers, femtosecond damage testing, laser-induced damage testing, LIDT testing

*K. R. P. Kafka, E-mail: kkaf@lle.rochester.edu

1 Introduction

Laser-induced damage of optics has long been recognized as an operationally limiting factor, constraining the amount of laser flux that optics can withstand. Practically, the size of the laser beam (and the corresponding optics) in an application must be large enough to provide sufficiently low laser flux to decrease the probability of damage to the optics. However, an increased beam size comes at increased resource cost, including manufacturing and installation of a new optic, refurbishing or repair of a damaged optic, and/or the inherent cost of system downtime. Therefore, a detailed knowledge of laser-induced–damage behaviors informs decisions on optic designs and choices and helps balance operational fluences against the costs within the budget constraints of a given laser system. Laser-induced–damage issues are particularly relevant for high-peak-power laser systems, which frequently employ large optics (up to meter scale) and operate at fluences near the onset of laser-induced damage.

The onset of damage initiation, referred to as the laser-induced–damage threshold (LIDT), has been the focus of the vast body of literature dedicated to the pursuit of this parameter.[1–7] A concentrated effort has been dedicated to develop universal standards for measurement.[8] Fundamentally, laser-induced–damage initiation requires sufficient absorption of the laser so that the material becomes permanently modified, often due an induced phase change such as melting or boiling. Since many optical materials are chosen to have low linear absorption properties within an application's operational spectral region, the onset of strong absorption and subsequent damage in short pulse laser systems is typically governed by nonlinear absorption dynamics and material inhomogeneities. The inhomogeneities cause a localized increase of absorption due to local modification of the electronic structure, and/or intensification of the electric field. Examples of inhomogeneities that are known to catalyze the initiation of laser-induced damage are material impurities or defects,[9] structural defects such as coating nodules,[10,11] contamination of the optical surface by particles or films,[12,13] and/or damage sites initiated by previous laser pulses.[14] In addition, many devices, such as those with multilayer dielectric coatings or diffraction gratings, employ engineered structures that introduce a distribution of electric-field intensification within its structure. In such devices, laser-induced–damage initiation is typically observed to correlate with locations that are subjected to the peak intensification.

While laser-induced damage governs the operational threshold in small-beam optics, large-aperture optics employed in the most powerful laser systems can operate using optics that have sustained some damage with limited performance degradation. Obviously, if a large fraction of an optic's area is damaged, the device is no longer functional to its desired specifications. On the other hand, in many high-quality devices, the number density of damage-catalyzing defects may be very low, such that the optic may continue to be effectively used even after suffering some

laser-induced–damage initiation. This continued use can be possible assuming that these sites do not grow (increase in size of the damaged area) under subsequent exposure to system laser pulses. In this regime, the operational lifetime of an optic then begins to be governed by the rate of damage growth as a function of the operational fluence. The threshold for damage growth has been shown to typically be less than the fluence for damage initiation (~50% for subpicosecond pulses[15]), consistent with the fact that existing damage-initiation sites act as damage-accelerating inhomogeneities. In general, growth rates are typically a function of fluence, and depend on the number of pulses (for fixed fluence exposure).[16]

To perform accurate measurements of damage growth parameters such as rate and threshold, the test beam must be significantly larger than the initial and subsequently growing damage site. Specifically, since damage growth is often caused by intensification of the laser in surrounding regions that involve the interference of the incoming and reflected or scattered waves, there must be sufficient illuminated area to generate this intensity distribution and allow the site to grow in irradiation conditions relevant to the operational environment (i.e., large-diameter slowly varying intensity profile). Furthermore, a larger beam enables a more-accurate assignment of fluence values as a function of position. Some LIDT-testing systems in the nanosecond pulse regime have optimized this approach by using multimillimeter-scale flattop beams.[17–19] Although technology exists to generate and transport large-diameter, high-energy, ultrashort laser beams, such an approach has not yet been fully implemented into damage testing systems with ultrashort pulses.

Laser-induced–damage research with femtosecond pulses has gained particular interest due to a new generation of multipetawatt-class ultrashort laser systems designed to provide high peak intensities on a target to study a plurality of effects across a broad range of disciplines including quantum electrodynamics and temporally resolving the electron dynamics in materials.[20–23]

In addition to traditional limitations imposed by laser-induced damage and damage growth, it has been shown that the optical properties of materials can be transiently modified under ultrashort-pulsed laser irradiation at below-LIDT fluences to such a degree that the functionality of a device may be modified/degraded or impeded.[24] In this case, the material often undergoes a transient and reversible change that modifies the refractive index during the laser irradiation. As a result, the function of the optic may be detrimentally modified even though the operational fluences are kept below the nominal LIDT. A limited set of studies has demonstrated these effects for the case of multilayer thin films with femtosecond pulses, finding different susceptibilities to laser-induced functional change for different types of coating designs.[24–26] However, this type of optic "failure" has not yet been adopted in laser-induced–damage testing systems.

The primary aim of this work is to provide a detailed description of a femtosecond laser-induced–damage testing system that not only meets existing ISO (International Organization for Standardization) standards regarding damage initiation measurement,[8] but also provides the capability to accurately quantify the damage growth threshold and provide functional performance characterization. Such enhanced capabilities are required to meet future needs emerging from current understanding and management of laser damage. A limited set of experimental results is shared as a demonstration of the capabilities of the system.

2 Characterization of ultrafast, large aperture optics

Ultrashort laser pulses (a few tens of femtoseconds in duration or less) have ultrawide spectral bandwidths and generate high intensities that necessitate proper management of the laser pulse's properties when designing and calibrating a system intended for optical performance characterization. Given that the LIDT is a fluence measurement that is a function of pulse duration,[27] the key laser parameters are pulse energy, spatial profile, and temporal profile. Some

potential calibration pitfalls are chromatic dispersion compensation, pulse contrast, and nonlinear phase shift (*B*-integral). Uncompensated chromatic dispersion due to propagation in air (meters) or transparent optics (millimeters) can have a significant effect on the pulse duration, with increasing impact for larger bandwidth. Even a pulse compressed to the Fourier transform limit could still be affected by poor contrast ratio, which could (at best) lead to an overestimate of LIDT due to significant energy distributed in satellite pulses or a pedestal. At worst, a poor pulse contrast interacting with a sample could behave as a pulse of a different shape or duration, causing the measurements to no longer match the intended test duration. The high intensity of a femtosecond laser can be vulnerable to nonlinear phase accumulation due to the Kerr effect during beam transport, which can modify the spectral bandwidth and/or spatial profile of the laser. Mitigation of such nonlinear effects is particularly important to measure damage growth, which requires large beams and, consequently, large pulse energies. Proper calibration of the system must be performed to ensure that the test laser pulse arriving at the sample has the desired properties for a given application.

An additional constraint for damage growth testing with ultrashort pulses is the need for variability of beam size. Laser-damage initiation with pulse durations less than ~3 ps canonically forms damage in a continuous region where the local fluence is above the LIDT,[28] resulting in site morphologies directly correlating with the size and shape of the test beam. To accurately measure damage growth requires an ability to properly adjust the beam size to provide irradiation that mimics that of a larger-aperture laser beam within the area (surrounding the damage site) involved by the damage growth process.

Given the above considerations, comprehensive performance characterization of optics must include, in addition to standard metrics of damage initiation, the metrics of damage growth and

laser-induced functional degradation. Ideally, a well-characterized laser system that is technically relevant to the intended operational parameters of the sample optics would be used to perform all related measurements. The desired capabilities of such a system include the following:

- Full capability for standard laser-induced–damage testing[8]
  - fluence measurement at equivalent sample plane
  - microscopic inspection for damage detection
  - pulse energy control, sufficient dynamic range (~10^1) extending above and below the LIDT value
  - pulse polarization control
  - ability to test at different angles of incidence.
- Damage-growth characterization
  - variable beam diameter, spanning at least an order of magnitude
  - expanded requirement for pulse energy dynamic range (>10^2), to achieve LIDT fluence across a range of beam sizes
- Laser-induced functional threshold (LIFT) characterization
  - diagnostic to measure and detect localized changes of a device's relevant functional parameter (reflectance, transmission, diffraction, etc.)
- Technical relevance and reliability
  - tunable spectrum, pulse duration, and test environment to reasonably cover intended operational parameters
  - accurate management and characterization of pulse compression, chromatic dispersion, and pulse contrast

– minimized nonlinear phase shift of system (B-integral $\lesssim 1$). Especially relevant for femtosecond lasers, important for larger test-beam sizes requiring larger pulse energy

The present work describes a system that was developed to meet these capabilities for near-infrared, femtosecond-pulsed applications.

3 Damage test system and apparatus

A schematic of the testing apparatus is shown in Fig. 1, with the main components consisting of an ultrafast laser and the experimental platform inside a vacuum. It employs a custom-built optical parametric chirped-pulse–amplification laser system ("Ultraflux," EKSPLA) with 20-fs pulse duration, 820-nm to 970-nm tunable central wavelength, 5-Hz repetition rate, and up to 2-mJ output pulse energy. The tunability of the spectrum provides a capability to characterize the performance of broadband near-infrared optics at different wavelengths within their operational band (which might be larger than that of the test system, e.g., to support shorter pulse durations). An acousto-optic programmable dispersive filter (AOPDF, "Dazzler," Fastlite) is integrated into the system, allowing a high degree of flexibility to fine-tune the pulse's spectral phase, and consequently the pulse duration. Example spectrum, temporal profile, and pulse contrast profile are shown in Fig. 2. Characterization of the temporal profile is performed with Spectral Phase Interferometry for Direct Electric-field Reconstruction (SPIDER, APE). Since the diagnostic was located outside the vacuum chamber (experiencing a different amount of total dispersion), the pulse compression needed to be fine-tuned for optimization at the experimental sample plane. To accomplish this, a 100-μm-thick beta-barium borate crystal for second-harmonic generation (SHG) was temporarily placed near the sample plane with the vacuum chamber pumped down to

10^{-5} Torr, and the second-order dispersion was adjusted in the AOPDF to maximize the SHG signal (minimizing pulse duration). If desired for experiments, the AOPDF could even be used to precisely detune the compression for performance characterization as a function of chirped-pulse duration. The system does not incorporate stabilization of the carrier envelope phase (CEP) since CEP fluctuations are expected to have negligible effects on laser-induced damage for this pulse duration with greater than six optical cycles. Regardless, any uncharacterized CEP effects would simply appear as statistical uncertainty in the damage results. A pulse contrast of about 10^6 has been measured with third-order cross-correlation (Sequoia, Amplitude Technologies). It is worth noting that all key aspects of the system (beam transport, energy control, focusing, polarization control, and diagnostics) must maintain functionality and alignment across the full tunable spectral range (including bandwidth) from about 760 nm to 1030 nm.

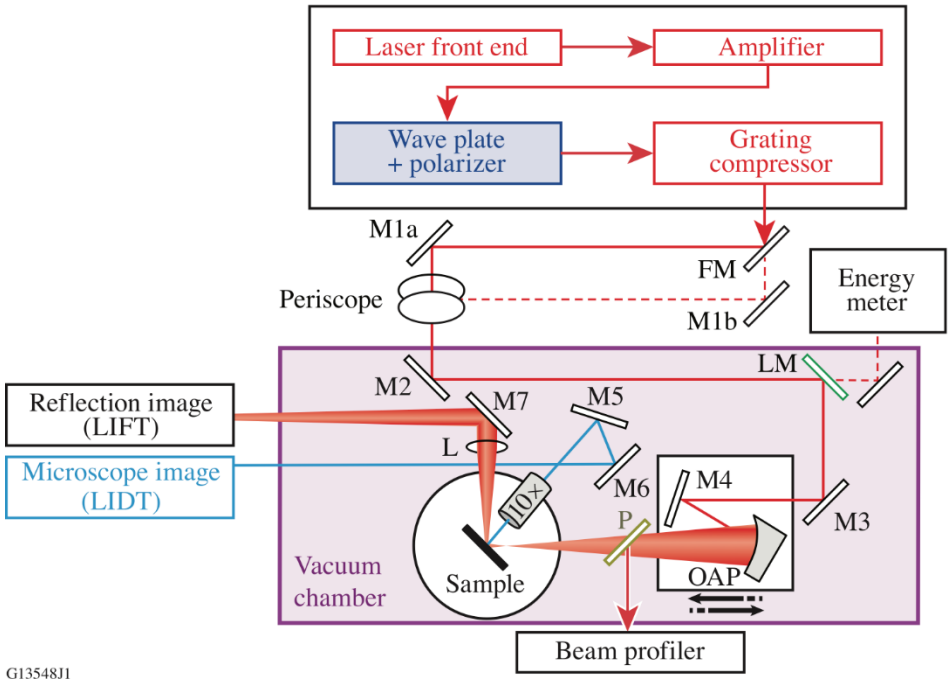

Fig. 1 Schematic of performance characterization apparatus. FM = flip mirror, M# = mirror, LM = leaky mirror, OAP = off-axis parabolic mirror, P = pickoff, 10× = 10× microscope objective lens, L = lens.

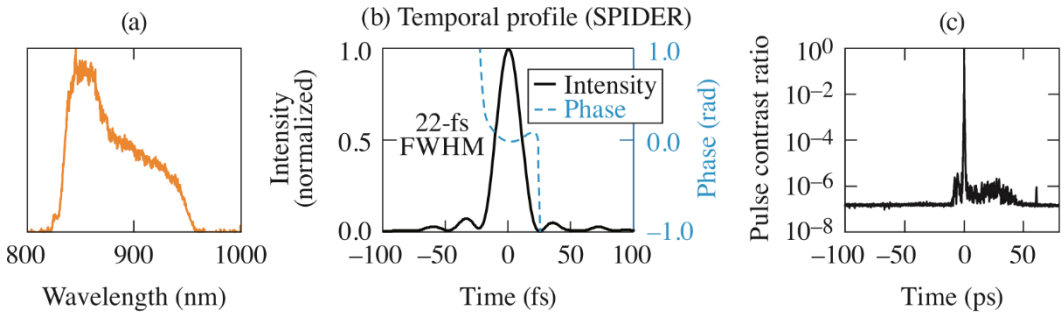

Fig. 2 Example temporal and spectral characteristics of the laser pulse: (a) spectrum, (b) temporal profile, and (c) pulse contrast.

Damage detection capability for standard laser-induced–damage testing is provided by an *in-situ* dark-field microscope. A low-power, 450-nm continuous-wave laser illuminates the targeted region of the sample, and an infinity-corrected long working distance 10× microscope objective lens (Mitutoyo) located inside the vacuum chamber relays the image of the sample surface onto a camera outside the chamber. The sample is mounted with six axes of motion control for alignment of the sample to the proper test plane, adjustment of angle of incidence, and for positioning to new sites during a test. Images of each site are saved before and after irradiation by the test laser, allowing for high-sensitivity damage detection via image subtraction. These features support typical damage testing protocols, such as S-on-1, R-on-1, and raster scanning.

In order to provide capability for variable beam size for damage growth characterization, the beam-focusing optic (off-axis-parabolic mirror, OAP in Fig. 1) is mounted on a translation stage together with folding mirror M4 to control the distance from the sample. As these two optics move in tandem, the beam size on the sample changes without disturbing beam alignment. The travel range of the stage is sufficient to provide $>10^1$ dynamic range of beam size, with the smallest focus about 60-μm Gaussian $1/e^2$ diameter. Example beam profiles of two different sizes are shown in Fig. 3(a) (at focus) and Fig. 3(b) (after the focus).

In a preliminary version of this system, the nonlinear phase shift (*B*-integral) had not yet been adequately managed, and the spatial profile was observed to be significantly distorted due to self-focusing when changing the output power by about two orders of magnitude. Although this distortion has since been adequately reduced, we share an example beam image from that version for instructional purposes [Fig. 3(c)]. Figure 3(d) is a difference image between the undistorted profile at low energy [Fig. 3(b)] and the distorted profile at high energy [Fig. 3(c)], where the profiles have been normalized to the total signal (unitless energy) in the low-energy profile. Clearly, the Kerr-lensing throughout the system diverted energy from the center of the beam toward larger radii, resulting in up to a 50% drop of fluence in the center of the distribution. This situation is not suitable for damage growth measurements; neither is it desirable for reliable LIDT measurements.

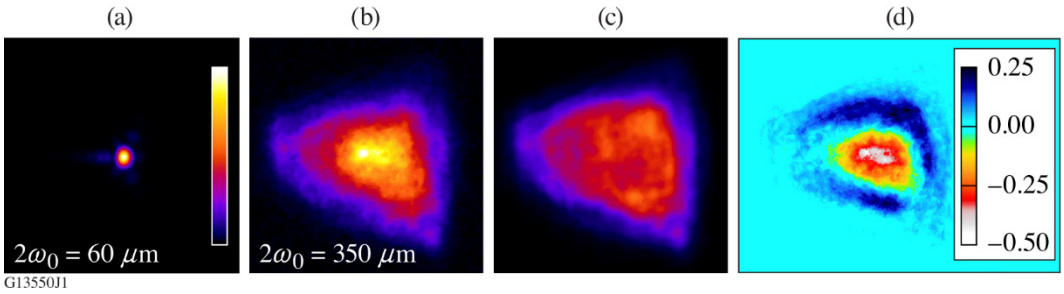

Fig. 3 Example beam spatial profiles: (a) at focal plane; (b) defocused larger beam intended for damage growth study; (c) example defocused profile that has been modified due to nonlinear phase accumulation at high pulse energy, measured before system was optimized; and (d) difference image of profiles (b) and (c).

The final design and implementation of the system minimized nonlinear phase as much as could be achieved without increasing the size of the beam during transport and without a vacuum pulse compressor, while maintaining all necessary operational variables. Nonlinear phase shift is typically expressed as $B = \frac{2\pi}{\lambda}\int n_2 I(z)\mathrm{d}z$, where λ is the laser wavelength, z is the position along the propagation

path, n_2 is the Kerr nonlinear refractive index of a transparent material, and $I(z)$ is the peak intensity of the beam. It is generally recommended for applications to keep the total accumulated phase through all elements after amplification to $B \lesssim 1$ in order to avoid significant spectral or spatial modulations [as seen in Fig. 3(c) for $B \approx 2$]. Practical strategies to minimize B include decreasing the path length (z) in materials, avoiding use of transparent optics after pulse compression when possible, increasing beam size during beam transport, and choosing transparent optical materials with a lower n_2 value. The subsequent paragraphs describe how these strategies were implemented.

In order to achieve high dynamic range of energy control ($>10^2$) so that near-LIDT fluences may be used across a wide range of beam sizes, the pulse energy reaching the sample is controlled by an achromatic half-wave plate and Glan polarizer. This post-manufacture module is located after the amplification stage inside the laser system, but is before the pulse compression stage. This approach maintains a negligible B-integral contribution because the pulse is still stretched by a factor of 10^3 longer pulse duration compared to laser output. A further advantage of this precompressor attenuation leverages the diffraction gratings of the compressor to further improve the extinction ratio, which is important since this broadband energy attenuation is the primary method of fluence adjustment during the damage-testing experiments. The extinction ratio of this module plus the gratings is $>10^3$, and even the maximally attenuated beam still maintains a polarization contrast $>10^3$ (wanted/unwanted polarization). All of the measurements in Fig. 3 have already included this stretched attenuation scheme since the thick polarizer alone would drive the B-integral well over 1 if it were placed after the compressor. The subsequently described engineering of the beam transport after the pulse compressor brought the total nonlinear phase shift down into a usable range, calculated to be around $B \approx 1$ at maximum pulse energy.

To control the polarization reaching the sample for testing, a rotatable periscope either maintains polarization or rotates it by 90° when combined with the corresponding one of two symmetric beam paths (see FM, M1a, and M1b in Fig. 1). This all-reflective geometry avoids the use of another achromatic wave plate, which has finite material thickness on the few-millimeter scale. A 3-mm-thick window of MgF_2 was used as the laser input port to the vacuum chamber, replacing the standard material of fused silica. MgF_2 is an excellent material for this application since it has approximately 3 to 4× lower n_2 value than fused silica,[29] as well as a slightly higher fracture toughness. The fracture toughness determines the minimum allowable window thickness to mechanically support the load of atmospheric pressure on one side when the chamber is pumped down to vacuum pressure. Therefore, MgF_2 can provide a similar minimum thickness to traditional fused silica while minimizing a major contributor to the total B.

A diagnostic pickoff (used for energy measurement and beam alignment reference) is performed with a broadband "leaky" mirror (LM in Fig. 1). The leaky mirror has a dielectric beam-splitter coating that transmits approximately 1% to 10% depending on polarization and spectral region. Again, this all-reflective solution reduces the total amount of material through which the compressed laser pulse must propagate. After the OAP, the laser beam passes through one transparent pickoff (P), which is only 1-mm-thick fused silica. The reflection from the uncoated back surface is used for equivalent-plane beam profiling (critical for fluence measurement), and it proved difficult to engineer without this optic. We note that a thin MgF_2 window is not suitable for this oblique-incidence beam sampler application due to birefringence. Overall, the total transparent bulk material after the compressor includes a vacuum window, a pickoff window, and about 3 m of air outside the chamber, which results in $B \approx 1$.

4 Example Measurements

The operation of the system is demonstrated by the testing of a low-group-delay-dispersion metal-dielectric mirror coating that is designed for broadband enhanced reflection in the near infrared. This coating design is also used on all the beam transport mirrors of this system. The mirror design consists of four quarter-wave dielectric layers: HfO_2, SiO_2, HfO_2, Al_2O_3, all on top of gold, designed for 45°, 15-fs operation and *p* polarization. This sample was tested at 890-nm central wavelength using 22-fs pulses at a 45° angle of incidence and *p* polarization under vacuum environment. Results of damage initiation and damage growth experiments are presented in Fig. 4. The damage-initiation measurement protocol was 1-on-1 procedure, irradiating each new test site with one pulse at a measured fluence, and damage probability was calculated using the "limit cumulative" method.[30] The damage growth measurements were carried out by first initiating damage sites using the smallest beam [60 μm, Fig. 3(a)] with a single pulse at a fluence 10% to 15% above the LIDT. This formed a damage site with a diameter of approximately 20 to 30 μm, a precursor from which to measure damage growth. Then the beam size was increased to 350-μm Gaussian diameter, and each precursor was irradiated by 50 pulses at a fixed fluence. Figure 5(a) depicts the size of the single-pulse damage initiation site with respect to the enlarged test beam. The remainder of Fig. 5 shows examples of nongrowing and growing sites with each test polarization, imaged off-line using differential interference contrast microscopy. Geometry of the laser incidence (from the left in Fig. 5), polarization, and the instantaneous size of the growing damage site after each exposure are all known factors that affect the multi-pulse damage growth morphology with femtosecond pulses.[14,31] Note that one must consider the nonuniformities of the beam profile when interpreting a growth morphology.

By comparing images of the sample before and after multipulse irradiation, the presence or absence of damage growth was determined for each site. The growth data were analyzed by the same probability method as the damage initiation. Each 1-on-1 test included 30 total sites, while each growth test included 15 sites. For the case of this sample, the *p*-polarized LIDT (0.45 J/cm^2) was less than the *s*-polarized LIDT (0.63 J/cm^2), but the *p*-polarized damage growth threshold (0.38 J/cm^2) was larger than the *s*-polarized damage growth threshold (0.24 J/cm^2). The uncertainty of these thresholds is approximately 0.02 J/cm^2. The ordering of these damage initiation and growth threshold values as a function of fluence is consistent with published results for an MLD mirror damaged by subpicosecond pulses,[14] and may be explained by differences in local electric-field intensity (EFI) experienced by the mirror for the different polarizations, with and without the presence of a pre-existing damage site. Future work will focus on the evolution of damage growth as a function of the excitation parameters and the design of the optic.

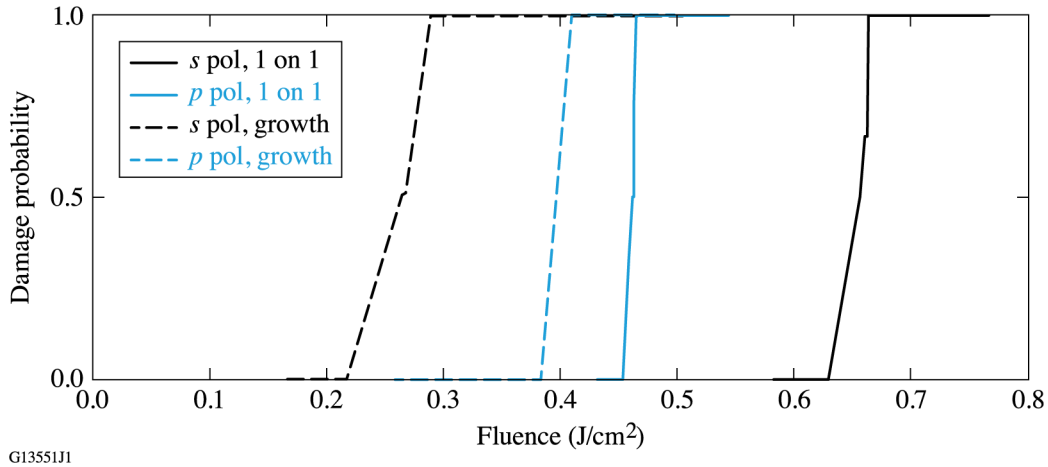

Fig. 4 Damage probabilities of damage initiation and damage growth on the metal-dielectric mirror sample.

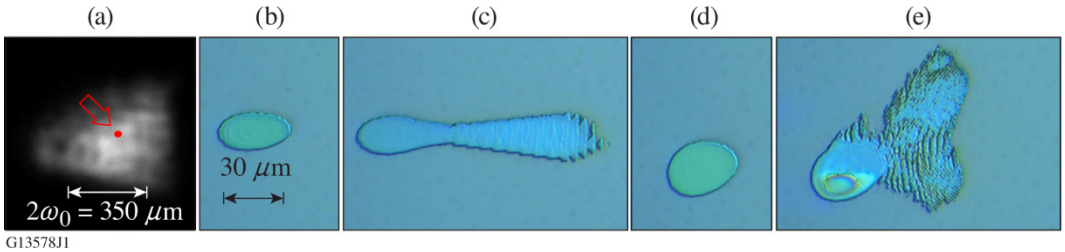

Fig. 5 Example morphologies of damage growth experiment in optical microscopy. (a) The 20- to 30-μm damage precursor is shown in red overlaid on an example beam profile. For *s*-polarization: (b) nongrowing site, (c) growing site at 0.34 J/cm^2. For *p*-polarization: (d) nongrowing site, (e) growing site at 0.43 J/cm^2. The laser is incident from the left.

The capability for LIFT measurement in this system is demonstrated by performing a characterization of the reflected beam from the metal-dielectric mirror sample surface. The reflected beam on the surface of the sample is imaged onto a camera located outside the chamber using an achromatic doublet lens and transport mirror (L and M7, respectively, in Fig. 1). A change of the reflection can be observed by calculating the ratio of reflected beam images from different pulses after first normalizing those images to the total energy. Specifically, reflected beam images represent the ratio between (1) a given test pulse and (2) a previous pulse that did not initiate damage.

An example sequence of ratio images showing a detected functional change is depicted in Fig. 6, alongside the concurrent images from *in-situ* dark-field microscopy that show damage has formed. The lineouts across the respective interaction regions are shown in Fig. 6(f). Starting with the pulse in Fig. 6(a), no damage is initiated, and the lineout shows a constant value. In Fig. 6(b), there is clearly a measurable drop of reflectance in the center of the laser beam (indicating functional failure), consistent with energy loss and the onset of damage. The dark-field images show before and after damage initiation [Fig. 6(d) and Fig. 6(e), respectively]. Since in this

example, the LIFT occurred concurrently to the initiation of damage, the ratio image from the next pulse [Fig. 6(c)] has severely reduced central reflectance (from 1.0 to 0.3) due to low reflectivity of the ablation site. This suggests that a system designed to measure LIFT could simultaneously be a sensitive *in-situ* diagnostic for LIDT measurement with *S*-on-1 or *R*-on-1 protocols.

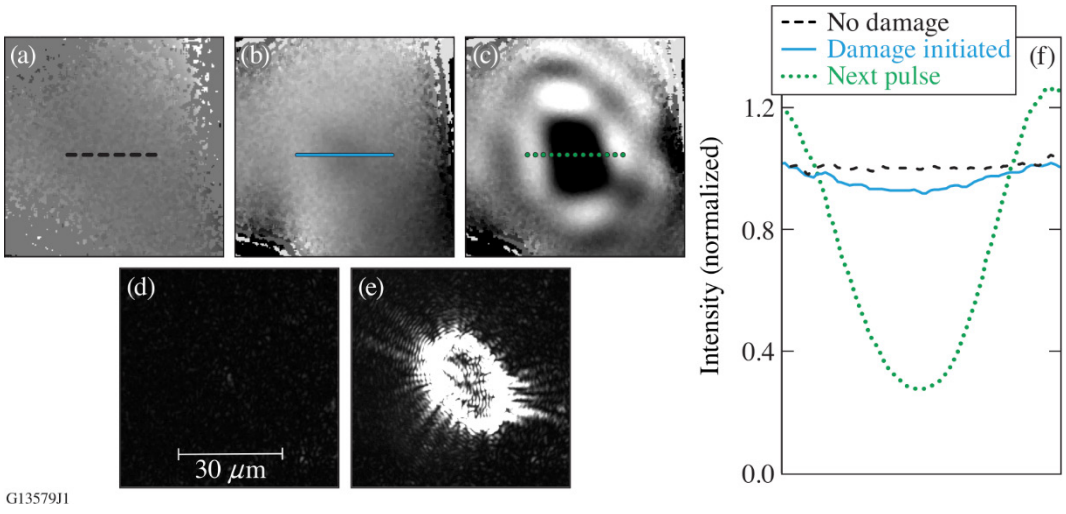

Fig. 6 *In-situ* microscopy of damage formation using (a–c), (f) functional performance characterization and (d,e) dark-field microscopy. Reflected beam images of (a) a pulse that did not damage, (b) the pulse that initiated damage, (c) the next pulse after damage initiation. Each image (a–c) was normalized by a reflected beam image of a previous pulse that did not initiate damage. (f) The lineouts of the respective reflection images. Dark-field microscope image of the sample, collected (d) before damage initiation, (e) after damage initiation but before the next pulse.

Analysis of laser-induced–damage testing data is classically complemented by imaging and analysis tools that help understand material modifications and their morphologies, which provide complementary information. The optimal use of that information is, in turn, directly related to the quality of the data. Next, we will briefly describe an extension of the study of the metal-dielectric mirror for the case of higher fluences. About 200 damage sites were generated at varying fluences to explore the damage-initiation threshold and damage-site morphology as a function of the input

fluence. These sites were subsequently characterized using atomic force microscopy (AFM), scanning electron microscopy (SEM) and an array of additional characterization tools including multispectral fluorescence microscopy, Raman scattering, and energy dispersive x-ray analysis. We will focus this discussion only on a specific aspect of the damage morphology that arguably provides insight into the damage-initiation conditions.

The lowest laser fluence where damage was observed was ≈0.46 J/cm^2 and manifested as crater with steep vertical walls. The bottom of the crater was within the top hafnia layer. With increasing fluence, the bottom of the crater migrated toward the interface of the top hafnia layer and the succeeding silica layer. With further increase of the fluence beyond about 0.6 J/cm^2, the damage site grows wider but not notably deeper, until the fluence reaches a value of about 1.3 J/cm^2. Figure 7 shows the depth of the crater as a function of the laser fluence, and Fig. 8 shows AFM profiles data for selected sites.

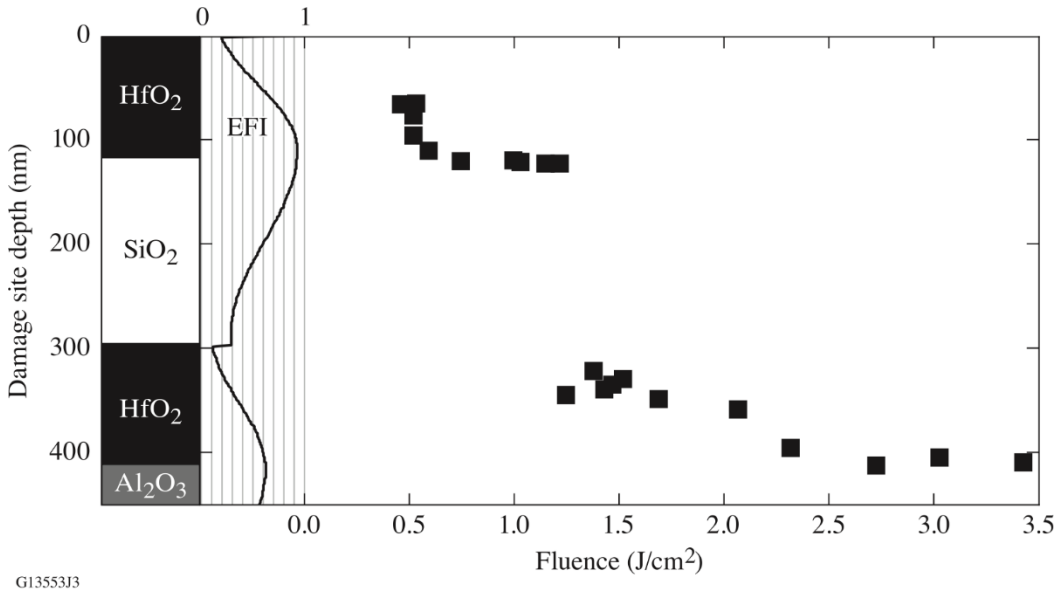

Fig. 7 The depth of the damage site crater on a metal-dielectric mirror as a function of laser fluence. To aid visualization, a depiction of the film layer arrangement and electric field intensity profile (EFI) is also shown.

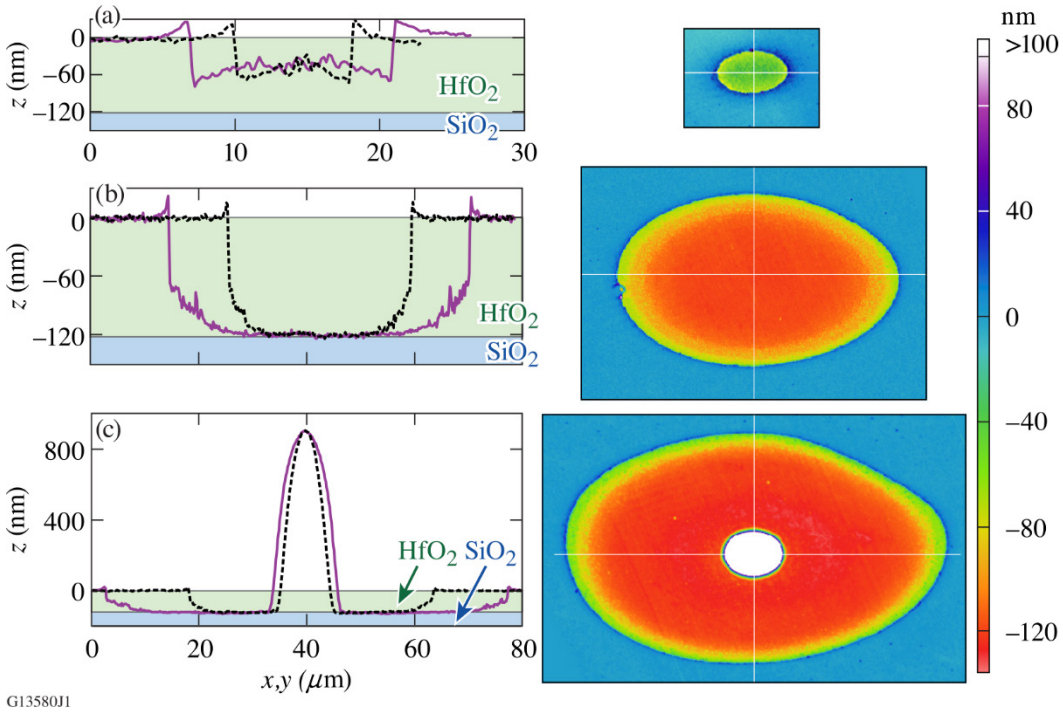

Fig. 8 AFM profiles and respective lineouts of one-pulse damage sites at fluences (a) 0.46, (b) 0.75, and (c) 1.2 J/cm^2.

Because of the much higher damage threshold of silica, the next damage initiation originates in the second hafnia layer. At a fluence just above 1.1 J/cm^2, a very tall blister sprouts out of the bottom of the crater (located near the hafnia and silica layer interface) and extends about 950 nm above the sample surface. At even higher fluence, this secondary blister erupts and exposes a second crater within the original crater with its bottom reaching the second hafnia layer, as shown in Fig. 8. Further increase of the laser fluence leads to migration of the bottom of the crater toward the interface with the alumina layer, which is reached at a fluence of about 2.7 J/cm^2.

Characterization of the damage sites provides insight on the thermomechanical processes involved in the damage site formation process. It is well established that damage initiation with ultrashort pulses is nearly deterministic and initiates at the location of local peak EFI of the layer that exhibits the lowest damage threshold (typically in hafnia), determined by the design of the

coating. Assuming that the crater depth coincides with the location of damage initiation, information on the local electric field strength can be obtained by monitoring the damage crater depth. Interestingly, in this experiment the exact depth of the crater does not correspond to the peak EFI location for either of the hafnia layers. Instead, the crater depths are shallower than the calculated EFI peak depths within the hafnia layers. This interaction is possibly governed in part by the plasma density and the transient change of the complex index of refraction, thus dynamically affecting the EFI distribution during the laser pulse and consequently the location of the damage initiation as well as the hydrodynamics of material ejection. Additional experiments and analysis in the future will be necessary to thoroughly understand these results. Nonetheless, monitoring the location and fluence of additional damage initiation at higher fluences has shown to provide complementary information on the damage initiation process and material response that can improve understanding of the process and influence the coating design. Such processes, if present, provide strong motivation for functional performance characterization measurements, and can be of great importance in developing a better understanding of the damage growth process and methods to mitigate it.

5 Conclusion

This work described optical engineering aspects required for the development of systems for ultrashort optical performance characterization that is more comprehensive than standard LIDT-testing stations, which primarily only characterize damage initiation. Specifically, the capability to characterize damage initiation, damage growth, and degradation of functional performance within a single system is targeted. An apparatus was presented that meets these capabilities for the near-infrared spectral regime, and an example case study of the metal-dielectric mirror demonstrated the system's functionality. Morphological analysis of the damage initiation sites

suggested a mismatch between the measured damage depths and the expected damage depths based on the coating design's EFI profile. The added capabilities of LIFT and damage growth characterization may provide additional insight into the mechanisms of this process in future work. The results underscore that precise damage-testing measurements of optical elements using ultrashort pulses and an expanded definition of damage is important to provide a wide range of information regarding the processes involved that can aid development of improved optic designs and reliable operational fluence limits.

Disclosures

The authors declare no conflicts of interest.

Acknowledgments

This material is based upon work supported by the Department of Energy National Nuclear Security Administration under Award Number DE-NA0003856, the University of Rochester, and the New York State Energy Research and Development Authority.

This report was prepared as an account of work sponsored by an agency of the U.S. Government. Neither the U.S. Government nor any agency thereof, nor any of their employees, makes any warranty, express or implied, or assumes any legal liability or responsibility for the accuracy, completeness, or usefulness of any information, apparatus, product, or process disclosed, or represents that its use would not infringe privately owned rights. Reference herein to any specific commercial product, process, or service by trade name, trademark, manufacturer, or otherwise does not necessarily constitute or imply its endorsement, recommendation, or favoring by the U.S. Government or any agency thereof. The views and opinions of authors expressed herein do not necessarily state or reflect those of the U.S. Government or any agency thereof.

421 *References*

422 1. P. K. Velpula, D. Kramer, and B. Rus, "Femtosecond laser-induced damage characterization of
423 multilayer dielectric coatings," *Coatings* **10**(6), 603 (2020).
424 2. P. K. Velpula, D. Kramer, M. Ďurák, and B. Rus, "Femtosecond laser damage resistance of beam
425 dump materials for high-peak power laser systems," *Opt. Eng.* **59**(5), 056108 (2020).
426 3. B. Mangote et al., "Femtosecond laser damage resistance of oxide and mixture oxide optical
427 coatings," *Opt. Lett.* **37**(9), 1478–1480 (2012).
428 4. A. Hervy et al., "Femtosecond laser-induced damage threshold of electron beam deposited dielectrics
429 for 1-m class optics," *Opt. Eng.* **56**(1), 011001 (2016).
430 5. C. B. Schaffer, A. Brodeur, and E. Mazur, "Laser-induced breakdown and damage in bulk transparent
431 materials induced by tightly focused femtosecond laser pulses," *Meas. Sci. Technol.* **12**(11),
432 1784–1794 (2001).
433 6. M. Mero, J. Liu, W. Rudolph, D. Ristau, and K. Starke, "Scaling laws of femtosecond laser pulse
434 induced breakdown in oxide films," *Phys. Rev. B* **71**(11), 115109 (2005).
435 7. Z. Sun, M. Lenzner, and W. Rudolph, "Generic incubation law for laser damage and ablation
436 thresholds," *J. Appl. Phys.* **117**(7), 073102 (2015).
437 8. ISO 21254-1:2011–ISO 21254-2:2011, "Lasers and Laser-Related Equipment–Test Methods for
438 Laser-Induced Damage Threshold," Part 1–2: Definitions and General Principles; Threshold
439 Determination (International Organization for Standardization, Geneva, Switzerland, 2011).
440 9. D. N. Nguyen, L. A. Emmert, P. Schwoebel, D. Patel, C. S. Menoni, M. Shinn, and W. Rudolph,
441 "Femtosecond pulse damage thresholds of dielectric coatings in vacuum," *Opt. Express* **19**(6),
442 5690–5697 (2011).
443 10. C. J. Stolz, M. D. Feit, and T. V. Pistor, "Laser intensification by spherical inclusions embedded
444 within multilayer coatings," *Appl. Opt.* **45**(7), 1594–1601 (2006).

11. X. Cheng, J. Zhang, T. Ding, Z. Wei, H. Li, and Z. Wang, "The effect of an electric field on the thermomechanical damage of nodular defects in dielectric multilayer coatings irradiated by nanosecond laser pulses," *Light Sci. Appl.* **2**(6), e80 (2013).
12. S. G. Demos et al., "Mechanisms governing the interaction of metallic particles with nanosecond laser pulses," *Opt. Express* **24**(7), 7792–7815 (2016).
13. K. R. P. Kafka et al., "Mechanisms of picosecond laser-induced damage from interaction with model contamination particles on a high reflector," *Opt. Eng.* **60**(3), 031009 (2020).
14. M. Sozet et al., "Sub-picosecond laser damage growth on high reflective coatings for high power applications," *Opt. Express* **25**(21), 25,767–25,781 (2017).
15. M. Sozet et al., "Laser damage growth with picosecond pulses," *Opt. Lett.* **41**(10), 2342–2345 (2016).
16. R. A. Negres et al., "Growth behavior of laser-induced damage on fused silica optics under uv, ns laser irradiation," *Opt. Express* **18**(19), 19,966–19,976 (2010).
17. L. M. Sheehan, M. R. Kozlowski, C. J. Stolz, F. Y. Genin, M. J. Runkel, S. Schwartz, J. Hue "Large-area damage testing of optics," *Proc. SPIE* **2775**, 357–369 (1996).
18. M. A. Norton et al., "Growth of Laser Damage in SiO_2 under Multiple Wavelength Irradiation," *Proc. SPIE* **5991**, 599108 (2005).
19. M. Veinhard, O. Bonville, R. Courchinoux, R. Parreault, J.-Y. Natoli, and L. Lamaignère, "MELBA: a fully customizable laser for damage experiments," *Proc. SPIE* **10447**, 104471U (2017).
20. J. M. Soures et al., "Direct-drive laser-fusion experiments with the OMEGA, 60-beam, >40-kJ, ultraviolet laser system," *Phys. Plasmas* **3**(5), 2108–2112 (1996).
21. S. Gales et al., "The extreme light infrastructure—nuclear physics (ELI-NP) facility: New horizons in physics with 10 PW ultra-intense lasers and 20 MeV brilliant gamma beams," *Rep. Prog. Phys.* **81**(9), 094301 (2018).
22. Z. Zhang et al., "The 1 PW/0.1 Hz laser beamline in SULF facility *High Power Laser Sci. Eng.* **8**, e4 (2020).

23. I. A. Begishev et al., "Advanced laser development and plasma-physics studies on the multiterawatt laser," *Appl. Opt.* **60**(36), 11,104–11,124 (2021).
24. O. Razskazovskaya et al., "Nonlinear behavior and damage of dispersive multilayer optical coatings induced by two-photon absorption," *Proc. SPIE* **9237**, 92370L (2014).
25. E. Fedulova et al., "Kerr effect in multilayer dielectric coatings," *Opt. Express* **24**(19), 21,802–21,817 (2016).
26. T. Amotchkina, M. Trubetskov, and V. Pervak, "Experimental and numerical study of the nonlinear response of optical multilayers," *Opt. Express* **25**(11), 12,675–12,688 (2017).
27. M. Lenzner, J. Krüger, S. Sartania, Z. Cheng, Ch. Spielmann, G. Mourou, W. Kautek, and F. Krausz, "Femtosecond optical breakdown in dielectrics," *Phys. Rev. Lett.* **80**(18), 4076–4079 (1998).
28. A. A. Kozlov et al., "Mechanisms of picosecond laser-induced damage in common multilayer dielectric coatings," *Sci. Rep.* **9**, 607 (2019).
29. T. R. Ensley and N. K. Bambha, "Ultrafast nonlinear refraction measurements of infrared transmitting materials in the mid-wave infrared," *Opt. Express* **27**(26), 37940–37951 (2019).
30. S. Schrameyer et al., "Algorithm for cumulative damage probability calculations in S-on-1 laser damage testing," *Proc. SPIE* **8885**, 88851J (2013).
31. Md. Rasedujjaman and L. Gallais, "Polarization dependent laser damage growth of optical coatings at the sub-picosecond regime," *Opt. Express* **26**(19), 24,444–24,460 (2018).

Kyle R. P. Kafka received his MS and PhD in Physics from the Ohio State University. Currently, he is a scientist at the Laboratory for Laser Energetics, University of Rochester, where his research interests include laser damage and material dynamics.

Tanya Z. Kosc received her Ph.D. from the Institute of Optics at the University of Rochester. She is a staff scientist at the Laboratory for Laser Energetics, University of Rochester.

494 **Stavros G. Demos** received his PhD in physics from City University of New York. He is a
495 distinguished scientist at the Laboratory for Laser Energetics, University of Rochester.

496
497
498 **Caption List**
499
500 **Fig. 1** Schematic of performance characterization apparatus. FM = flip mirror, M# = mirror, LM
501 = leaky mirror, OAP = off-axis parabolic mirror, P = pickoff, 10× = 10× microscope objective
502 lens, L = lens.
503 **Fig. 2** Example temporal and spectral characteristics of the laser pulse: (a) spectrum, (b) temporal
504 profile, and (c) pulse contrast.
505 **Fig. 3** Example beam spatial profiles: (a) at focal plane; (b) defocused larger beam intended for
506 damage growth study; (c) example defocused profile that has been modified due to nonlinear phase
507 accumulation at high pulse energy, measured before system was optimized; and (d) difference
508 image of profiles (b) and (c).
509 **Fig. 4** Damage probabilities of damage initiation and damage growth on the metal-dielectric mirror
510 sample.
511 **Fig. 5** Example morphologies of damage growth experiment in optical microscopy. (a) The 20- to
512 30-μm damage precursor is shown in red overlaid on an example beam profile. For *s*-polarization:
513 (b) nongrowing site, (c) growing site at 0.34 J/cm^2. For *p*-polarization: (d) nongrowing site, (e)
514 growing site at 0.43 J/cm^2. The laser is incident from the left.
515 **Fig. 6** *In-situ* microscopy of damage formation using (a–c), (f) functional performance
516 characterization and (d,e) dark-field microscopy. Reflected beam images of (a) a pulse that did not
517 damage, (b) the pulse that initiated damage, (c) the next pulse after damage initiation. Each image
518 (a–c) was normalized by a reflected beam image of a previous pulse that did not initiate damage.

519 (f) The lineouts of the respective reflection images. Dark-field microscope image of the sample,
520 collected (d) before damage initiation, (e) after damage initiation but before the next pulse.
521 **Fig. 7** The depth of the damage site crater on a metal-dielectric mirror as a function of laser fluence.
522 To aid visualization, a depiction of the film layer arrangement and electric field intensity profile
523 (EFI) is also shown.
524 **Fig. 8** AFM profiles and respective lineouts of one-pulse damage sites at fluences (a) 0.46, (b)
525 0.75, and (c) 1.2 J/cm^2.
526